

# Stochastic Equilibrium Raman Spectroscopy (STERS)

COLBURN COBB-BRUNO<sup>1</sup> AND HENDRIK UTZAT<sup>\*1,2,3</sup>

<sup>1</sup>*Department of Chemistry, University of California Berkeley, 200 Centennial Drive Berkeley, California 94720, USA*

<sup>2</sup>*Materials Science Division, Lawrence Berkeley National Lab, Berkeley, California 94720, USA*

<sup>3</sup>*hutzat@berkeley.edu*

**Abstract:** We theoretically propose a new method in cavity- and surface-enhanced Raman spectroscopy (SERS) with improved temporal resolution in the measurement of stochastic Raman spectral fluctuations. Our approach combines Fourier spectroscopy and photon correlation to decouple the integration time from the temporal resolution. Using statistical optics simulations, we establish the relationship between time resolution and Raman signal strength, revealing that typical Raman spectral fluctuations, commensurate with molecular conformational dynamics, can theoretically be resolved on micro- to millisecond timescales. The method can further extract average single-molecule dynamics from small sub-ensembles, thereby potentially mitigating challenges in achieving strictly single-molecule isolation on SERS substrates.

## 1. Introduction

Raman spectroscopy is a ubiquitous tool in many fields of science most commonly used to determine molecular structure and materials' phonon dispersion [1]. Peak *shifts* in Raman spectroscopy can also be used to measure ionic strength, temperature, and material deformation. [2, 3] Of particular interest in the chemical sciences are spectral shifts induced by intra- and intermolecular interactions, including molecular stacking, straining, or solvation. [4–8] Such Raman shifts have been used, for example, to distinguish between healthy and diseased states of biological tissue and to detect biomolecular binding events, but largely statically. [8–12] A long-standing proposal has been to use time-resolved single-molecule Raman spectroscopy to access chemical and biophysical dynamics such as surface adsorption/desorption, biomolecular binding/unbinding, protein conformational changes, or stochastic molecular charging in the absence of heterogeneous broadening. [8, 11, 13–15] This goal is limited by low Raman cross sections that require surface enhancement to achieve single-molecule sensitivity. High-enhancement plasmonic substrates can interfere with the native analyte dynamics, rendering single-molecule or subensemble Raman studies challenging and often inconsistent. In cases where SERS can resolve single molecules, [13, 16–25] low signal strength (Raman photons/second) compared to fluorescence currently limits the achievable time resolution. The resolution of generic frame-by-frame SERS based on diffraction gratings typically extends into the millisecond range, fundamentally limited by photon shot noise, leaving timescales faster than the photon count rate uncovered. [13, 16, 20, 22, 23] At the other extreme of timescales, ultrafast vibrational spectroscopy can reveal ensemble vibrational dynamics, e.g., through two-dimensional IR spectroscopy, femtosecond stimulated Raman spectroscopy, or surface-enhanced infrared absorption spectroscopy (SEIRA). [26] However, these methods largely lack the ability to discriminate between the behavior of sub-ensembles or single molecules. [19, 27–29] Critically, both frame-by-frame SERS and ultrafast Raman/IR methods generally struggle to resolve nanosecond-to-millisecond dynamics, which are critical in many molecular systems. Although recent work motivated by the need to understand surface-atom dynamics was able to resolve microsecond spectral shifts, this has only been achievable with the highest possible SERS enhancement factors from extreme field confinement in plasmonic gap cavities. [20, 30, 31] Such plasmonic gap cavities do not permit the investigation of unperturbed temporal fluctuations

in the molecular Raman shift of larger analytes, e.g., single biomacromolecules. As a result, new methods to reveal single-molecule dynamics from faint SERS signals obtained from low-enhancement structures with a high temporal dynamic range would be valuable.

In this concept paper, we explore a new way to conduct SERS experiments to address two current challenges: (1) the limited time resolution due to low SERS signals and (2) the ambiguity in distinguishing single- versus few-molecule Raman spectral dynamics. We introduce our method, Stochastic Equilibrium Raman Spectroscopy (STERS), and theoretically and numerically explore the expected analytical figures of merit for analyzing STERS dynamics. STERS correlates Raman photon energies based on their time separation. In ergodic systems, temporal correlation functions quantify average changes between two time points. In spectroscopy, the spectral correlation function measures how much, on average, an optical spectrum shifts in frequency over a given period. Therefore, as long as Raman spectral fluctuations are ergodic over the course of the experiment, the spectral correlation function  $p(\tau, \zeta)$  can be used to quantify the timescale and amplitude of spectral dynamics, where  $\tau$  is the lag time between photons,  $\zeta$  is the energy difference between two scattered photons, and  $\langle \dots \rangle$  denotes a time average:

$$p(\tau, \zeta) = \left\langle \int_{-\infty}^{\infty} s(t, \omega) s(t + \tau, \omega + \zeta) d\omega \right\rangle. \quad (1)$$

Spectral diffusion dynamics are extracted from the evolution of the spectral correlation as a function of  $\tau$ . Figure 1 illustrates the spectral correlation observable through simulations (the details are discussed in the results section). Analyzing dynamics can for example be accomplished by tracking the width of the spectral correlation over  $\tau$  as shown in Figure 1 b. The spectral correlation approach bears the general advantages of high spectral and temporal resolution/temporal dynamic range. These figures of merit cannot be simultaneously optimized with grating-based Raman spectroscopy.

This general concept was introduced earlier in Photon-Correlation Fourier Spectroscopy (PCFS) to measure the spectral diffusion in single emitter electronic transitions. [32] In short, time-stamped photon detection is performed with two photon counting detectors at the output arm of a scanning Michelson interferometer (Figure SI 1). The  $g^2(\tau)_\delta$  auto- and cross-correlation functions are determined at different interferometer pathlength differences across the emitter’s coherence length. The Fourier Transform of  $g^2(\tau)_\delta$  from path-length difference to energy difference gives the spectral correlation  $p(\zeta, \tau)$ . While PCFS has been used in different situations at low and room temperature, [33–35] we propose that the translation to single and few-molecule Raman is particularly powerful because the spectral correlation can quantify vibrational spectral diffusion originating from relevant local dynamics.

In this context, an important question is whether typical vibrational spectral diffusion can in principle be resolved. We address this through numerical simulations to determine the expected analytical figures of merit—primarily temporal resolution and temporal dynamic range—for parameterized spectral diffusion models and low photon count rates. We then contextualize these simulations within real measurement challenges and propose STERS as a promising approach for measuring multi-timescale Raman spectral diffusion as a proxy for chemical and biophysical dynamics.

## 2. Simulation Results

We parameterize stochastic Raman spectral fluctuations using two phenomenological models and perform statistical optics Monte Carlo simulations, employing experimentally informed parameters for the Raman lineshape and signal strength. These simulations assume a shot-noise-limited measurement with variable photon count rates. The two models describe the discrete stochastic jumping of a Raman line between different center frequencies and with a characteristic time constant  $\tau_c$  [36, 37].

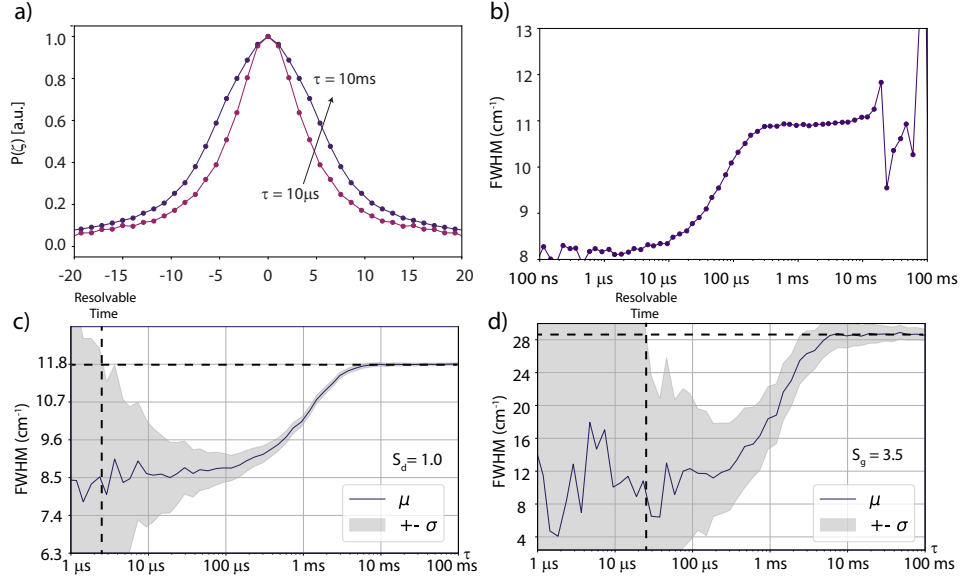


Fig. 1. Simulated plots introduce the spectral correlation and how we define resolvability. (a) shows the spectral correlation at select  $\tau$  values. (b) shows the FWHM evolution with  $\tau$  illustrating a spectral fluctuation at  $100 \mu\text{s}$ . (c) and (d) show the FWHM evolution over  $\tau$  with the standard deviation obtained via 100 consecutive simulations. (c) uses  $S_d = 1$  and 1000 photons per second and (d) uses  $S_g = 3.5$  with 100 photons per second. The experimental time was 5 hours in both cases.

In the 'two-state model' (Figure 2 b, inset), the center frequency of the Lorentzian lineshape alternates between two spectrally shifted states, representing scenarios such as switching between two discrete conformations. Line broadening progresses from the intrinsic lineshape

$$s(\omega) = \frac{\frac{1}{\Gamma}}{\frac{1}{\Gamma^2} + (\omega - \omega_{1,2})^2}, \quad (2)$$

to the diffused lineshape

$$s(\omega) = \frac{\frac{1}{\Gamma}}{\frac{1}{\Gamma^2} + (\omega - \omega_1)^2} + \frac{\frac{1}{\Gamma}}{\frac{1}{\Gamma^2} + (\omega - \omega_2)^2}. \quad (3)$$

In the 'Gaussian model' (Figure 2 a, inset), discrete spectral jumps occur within a Gaussian frequency probability distribution, mimicking a continuous distribution of possible states. This model results in a broadened lineshape with the general form of

$$s(\omega) = \int_{-\infty}^{\infty} e^{-\frac{1}{2}(\frac{\omega' - \mu}{\sigma})^2} \frac{\frac{1}{\Gamma}}{\frac{1}{\Gamma^2} + (\omega - \omega')^2} d\omega', \quad (4)$$

and the intrinsic lineshape

$$s(\omega) = \frac{\frac{1}{\Gamma}}{\frac{1}{\Gamma^2} + (\omega - \omega')^2}. \quad (5)$$

Both models are parameterized in their Lorentzian linewidth  $\Gamma$ . For the Gaussian model, the width of the spectral jumping probability distribution is defined by  $\sigma$ . For the two-state model, the spectral separation between the two states is given by  $\Delta\nu = |\omega_1 - \omega_2|$ , functionally replacing  $\sigma$ . As in other spectral shift measurements, the resolvability of STERS depends on the ratio of the intrinsic linewidth to the broadened linewidth. We introduce the parameters  $S_d \equiv \frac{\Delta\nu}{\Gamma}$  for the two-state model and  $S_g \equiv \frac{\sigma}{\Gamma}$  for the Gaussian model to quantify the relative magnitude of dynamic linewidth broadening. These parameters effectively measure how much the intrinsic Raman lineshape is broadened due to spectral diffusion. The stochastic model for Spectral diffusion can be found in [38].

In the following, we simulate the spectral correlation for select cases of  $S_{d,g}$ . We then discuss the results in the context of estimated  $S_d$  and  $S_g$  derived from published experimental work.

### 2.1. Quantification of Raman Spectral Diffusion Using STERS

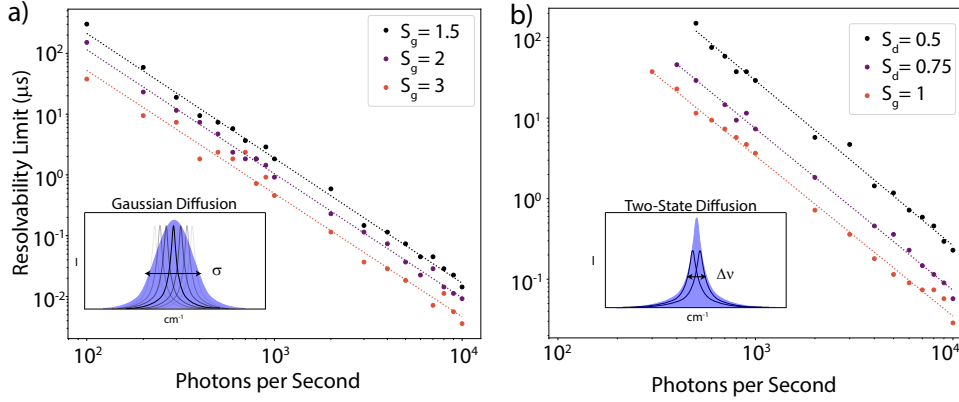


Fig. 2. Simulated results of the resolvability for different  $S_{d,g}$ . The insets show an illustration of each diffusion model.

First, we explore the ability of STERS to resolve small relative magnitude spectral fluctuations ( $0.5 < S_{d,g} < 3$ ) of one isolated and spectrally diffusing Raman line. Our main objective is to identify the achievable time resolution for low photon count rates for different  $S_{d,g}$ . In brief, Poisson temporal photon streams are generated with statistically drawn frequencies and mapped onto virtual detectors based on photon frequency and interferometer position. [38] STERS analysis is then performed on this virtual photon-counting data. A center Raman mode frequency of  $1106 \text{ cm}^{-1}$ , e.g. characteristic of an aromatic ring breathing mode, was chosen. This choice of the Raman Stokes wavelength affects the delay stage motion parameters in our simulations, but it does not impact the final spectral correlation, which only depends on the linewidth and spectral diffusion and is always centered at  $\zeta = 0$  and in practice, any sufficiently bright Raman line can be analyzed with STERS. The intrinsic linewidth  $\Gamma$  used in the simulations is  $4 \text{ cm}^{-1}$ , an estimate from [17, 39]. The details of these simulations are discussed in the Methods section.

Representative simulation results are shown in Figure 1 c,d. The grey area around the mean represents the standard deviation of the full width at half maximum (FWHM) of  $p(\zeta, \tau)$ , obtained from 100 consecutive simulations. Spectral diffusion may still be resolved as long as the observed spectral correlation broadening exceeds the uncertainty of the measurement. For the sake of our discussion, we therefore define the achievable time resolution for a given  $S_{d,g}$  as the value of  $\tau$  where the FWHM uncertainty starts to exceed the broadening. This is illustrated

in Figure 1 c,d where the resolvability would be  $\sim 4\mu\text{s}$  and  $\sim 15\mu\text{s}$ , respectively, and indicated by vertical dashed lines.

The achievable resolvability in this shot-noise limited correlation measurement depends on the total number of photon pairs collected with a given  $\tau$ . Our simulations assess the achievable resolution for different  $S_{g,d}$ , reasonably high total experiment times (five hours) and variable rates of Raman signal photons per second per molecule (100 to 10,000). The chosen  $S_g$  for the Gaussian model are 1.5, 2, and 3 (Figure 2), and  $S_d$  for the two-state model are 0.5, 0.75, and 1 (Figure 2 b). Values of  $S_d > 1$  are excluded as the spectral correlation adopts a triplet lineshape, requiring different fitting of the spectral correlation and revised definition of the shown FWHM. This is justified by our focus on low-amplitude spectral diffusion. The resolvability of a fluctuating Raman mode that follows a Gaussian diffusion model ranges from  $\sim 100\mu\text{s}$  with 100 Raman photons per second per molecule to  $\sim 10\text{ ns}$  with 10,000 photons per second per molecule in our chosen range of  $S_g$ . Comparing with  $S_d$  in Figure 2 b reveals a tenfold lower time resolution for similar photon counts for the two-state model, thereby defining a range for the expected resolvability for different diffusion models.

## 2.2. Resolution of Multi-Timescale Dynamics

STERS can furthermore resolve temporally distinct spectral fluctuations in the same spectral line, for example of the form  $s(\omega, t) = s(\omega)_0 + \delta s(\omega(t))_1 + \delta s(\omega(t))_2$ , where the two fluctuation terms  $\delta s(\omega(t))_{1,2}$  can possess different amplitudes and characteristic diffusion times. We illustrate this ability through a simulation of two independent spectral diffusion sources with  $S_d = 0.25$  and  $0.5$  and characteristic spectral shift times  $\tau_c$  of  $10\mu\text{s}$  and  $1\text{ ms}$  shown in Figure 3. We propose similar parameters could arise from a scatterer traversing a potential energy surface with four wells, each corresponding to a different mode frequency, and a total of four forward- and backward transition rates. Like in fluorescence correlation spectroscopy (FCS), only the faster characteristic transition rate of each forward- and backward pair will show in the spectral correlation because fast broadening of  $p(\zeta, \tau)$  obscures any slower broadening of the same amplitude. [40] This leads to the evolution of the FWHM of  $p(\zeta, \tau)$  with two distinct fluctuation times,  $\tau_{c1}$  and  $\tau_{c2}$ , shown in Figure 3 b.

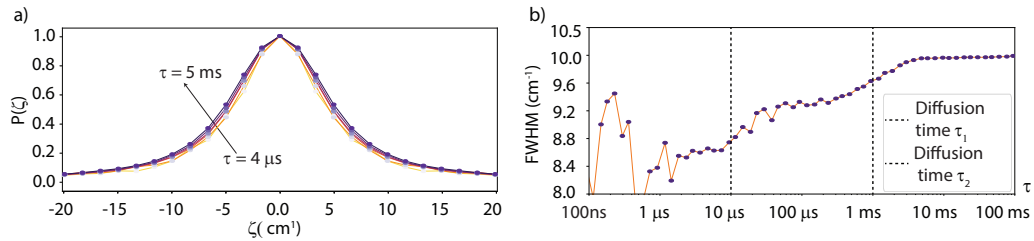


Fig. 3. Simulated plots illustrate two intrinsic fluctuation timescales. (a) shows the spectral correlation at select  $\tau$  values, while (b) shows the FWHM evolution over time. The simulation was run with 1000 photons per second, an intrinsic linewidth of  $4\text{ cm}^{-1}$ , and two discrete spectral jumps of  $S_d = 0.25$  and  $0.5$ , with  $\tau_c = 10\mu\text{s}$  and  $1\text{ ms}$ . The intrinsic Lorentzian width was  $4\text{ cm}^{-1}$ .

## 2.3. Obtaining Average Single-Molecule Raman Dynamics from Sub-Ensembles

Isolating, verifying, and measuring SERS from a single molecule (or analyte particle) is still challenging with conventional methods. [41] Similar to FCS, STERS can measure average single-molecule dynamics from a sub-ensemble, eliminating the effect of inhomogeneous broadening. This both avoids the difficulty of strictly single molecule observation and may allow

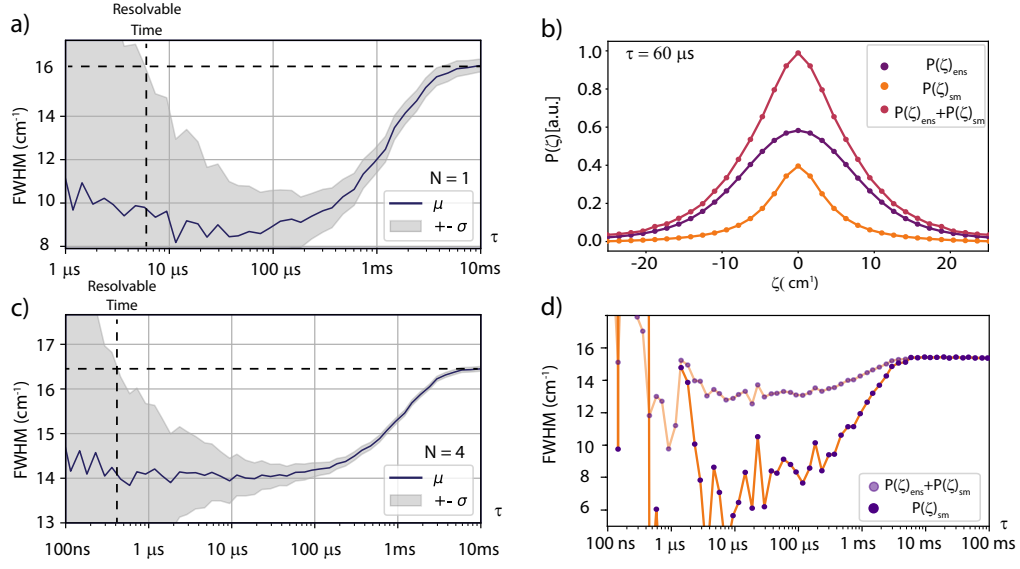


Fig. 4. Evolution of the spectral correlation for over  $\tau$  for ensemble size  $N = 1$  (a) and  $N = 4$  (c) with  $\tau_c = 1$  ms. a) and c) were simulated with 10,000 photons per second for a total experimental time of 30 minutes. The means and error bars were computed from 100 different simulations. b) shows the spectral correlation for an ensemble size four fitted to a diffused Voigt profile and a Lorentzian representing the ensemble and the single molecule spectral correlation respectively given the relationship in Eq. (7). d) shows the FWHM evolution for the ensemble and the single molecule spectral correlation components from b). b) and d) were simulated for 5 hours of total experimental time. All plots correspond to a value of  $S_g = 2$

single-molecule analysis with less complex or inconsistent sample preparation, e.g., by using larger mode volume nanocavities hosting sub-ensembles of molecules. As the correlation of an ensemble of independent spectral diffusers separates into auto- and cross-correlations, the total spectral correlation can be written in terms of ensemble and average single molecule components:

$$p(\zeta, \tau) = p(\zeta, \tau)_{\text{single molecule}} + p(\zeta)_{\text{ensemble}}, \quad (6)$$

where  $p(\zeta)_{\text{ensemble}}$  is  $\tau$ -invariant. It can therefore simply be subtracted from the total spectral correlation to obtain the  $\tau$ -dependent  $p(\zeta, \tau)_{\text{single molecule}}$ . We provide further derivations and explanations in the SI. The signal-to-background ratio (SBR) decreases with increasing number  $N$  of molecules under observation. With  $p(\zeta)_{\text{ensemble}}$  as the background and  $p(\tau, \zeta)_{\text{single molecule}}$  as the signal, the SBR can be expressed as:

$$SBR = \frac{p(\zeta, \tau)_{\text{single molecule}}}{p(\zeta)_{\text{ensemble}}} = \frac{1}{N - 1}, \quad (7)$$

which is undefined for  $N = 1$  with zero. This relationship is also seen in solution phase FCS. [42] The experimental observable for a small ensemble is shown in Figure 4, simulating spectral correlation for a single molecule ( $N=1$ ) and a small ensemble ( $N=4$ ) with independently diffusing emitters ( $S_g = 2$ ). Comparing Figure 4 a and Figure 4 c reveals that for  $N=1$  and  $N=4$ , the spectral correlation width increases by  $\approx 8 \text{ cm}^{-1}$  and  $\approx 2.4 \text{ cm}^{-1}$ , respectively. The smaller relative increase for larger ensemble sizes is due to the larger contribution of the  $\tau$ -invariant  $p(\zeta)_{\text{ensemble}}$  to the overall  $p(\tau, \zeta)$ .

By fitting the spectral correlation to an ensemble and single molecule correlation, the single molecule component  $p(\zeta, \tau)_{\text{single molecule}}$  can be obtained from the sum spectral correlation. Figure 4 b shows this decomposition into  $p(\zeta)_{\text{ensemble}}$  with a Voigt lineshape profile and  $p(\tau, \zeta)_{\text{single molecule}}$  with Lorentzian shape. Figure 4 d compares the  $\tau$ -dependent FWHM of the total spectral correlation extracted average single-molecule component. We note that while the amplitude of  $p(\tau, \zeta)_{\text{single molecule}}$  decreases with increasing  $N$ , the shot noise on both  $p(\tau, \zeta)_{\text{single molecule}}$  and  $p(\zeta)_{\text{ensemble}}$  decreases due to a higher total photon count rate. Therefore,  $p(\tau, \zeta)_{\text{single molecule}}$  can in principle be obtained for high  $N$ . [42]

## 2.4. Multi-Dimensional Cross-Correlation STERS

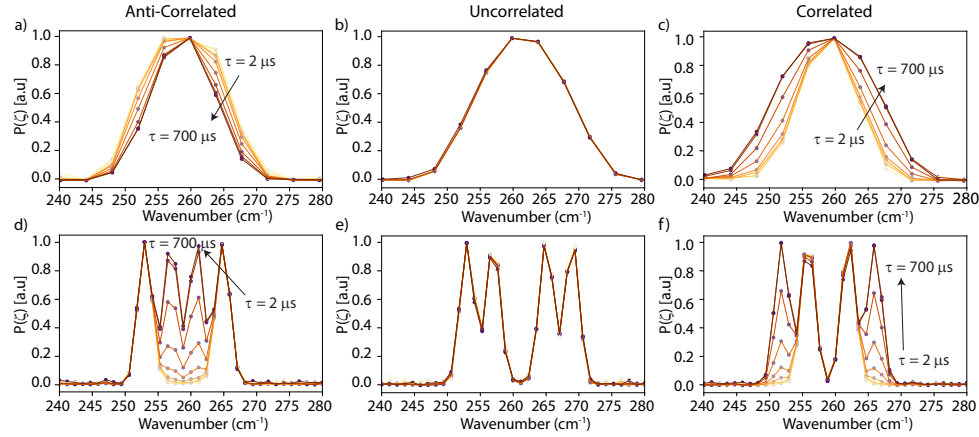


Fig. 5. Illustration of the Multi-Dimensional SFRS observable. The columns from left to right correspond to anti-correlated, uncorrelated, and correlated frequency fluctuations. Two Raman modes at  $847$  and  $1106 \text{ cm}^{-1}$  were used. The simulations in a), b), and c) were simulated with an intrinsic linewidth of  $1.5 \text{ cm}^{-1}$  with switching frequency magnitudes of  $4 \text{ cm}^{-1}$  and  $5 \text{ cm}^{-1}$  ( $S_d = 2.67, 3.33$ ) at a characteristic fluctuation time of  $\tau_{c1} = 100 \mu\text{s}$ . c), d), and e) were simulated with a linewidth of  $4 \text{ cm}^{-1}$  with the same fluctuational parameters ( $S_d = 1, 1.25$ ).

The discussion above primarily focuses on resolving the diffusion of a single Raman line. However, multi-dimensional correlation analysis across different Raman lines naturally provides more information about system fluctuations. Distinctly correlated, anti-correlated, or uncorrelated frequency fluctuations have been observed on timescales of seconds and picoseconds [43, 44]. STERS can resolve similar frequency cross-correlations between distinct Raman lines on intermediate timescales. Figure 5 illustrates how correlated, uncorrelated, and anti-correlated Raman spectral fluctuations between two modes manifest in the STERS spectral correlation. As an example, we consider two phenomenological modes at  $847$  and  $1106 \text{ cm}^{-1}$ , corresponding to the C-O stretching and ring-breathing modes of tyrosine [45]. In general, the qualitative features of  $p(\zeta, \tau)$  remain similar for any two modes with different absolute center energies.

The general shape of the multi-dimensional spectral correlation is shown in Figure 5 a-c. For two modes that are anti-correlated, the spectral correlation evolves from a wide doublet into a quartet (Figure 5 a), whereas for two correlated modes, it evolves from a narrow doublet into a quartet (Figure 5 c). Two uncorrelated modes show no change, as seen in Figure 5 b. For smaller linewidth/shift ratios, instead of transitioning from a doublet to a quartet through broadening or narrowing, the spectral correlation appears as a single peak that broadens and narrows for

correlated and anti-correlated fluctuations, respectively (Figure 5 d,f). Again, uncorrelated modes show no change. The broadening and narrowing behavior arises because, for anti-correlated modes, the energy difference is maximal before  $\tau_c$  and decreases for  $\tau > \tau_c$ , narrowing the spectral correlation. For correlated modes, the trend reverses, leading to spectral broadening.

### 3. Discussion

STERS builds on a previous method, Photon Correlation Fourier Spectroscopy (PCFS) [32], and constitutes the first application to cavity- and surface-enhanced Raman spectroscopy. Based on our simulations above, we propose distinct advantages of STERS, which we discuss by contextualizing the simulations with existing methods and microscopic mechanisms causing vibrational spectral diffusion with specific amplitudes and characteristic times.

STERS eliminates the trade-off between spectral resolution and signal throughput using grating spectrometers. Because STERS gains temporal resolution through energy-time correlation analysis (sacrificing the absolute energy of photons), it can help fill the current measurement gap in single-molecule vibrational spectroscopy from nanoseconds to milliseconds, challenging for pump-probe and frame-by-frame methods. On these timescales, fluctuations in the local electric field strength, adsorption geometry, biomolecular conformational structure, and molecular interactions contribute to dynamic Raman linewidth broadening. [2, 3, 8–12] Studies that unequivocally delineate these mechanisms at the level of single molecules are scarce, but a range for expected  $S_d, g$  may be considered.

An upper limit for the expected  $S_g$  may be obtained from inhomogeneous broadening. At low temperatures, variations in the Raman line center energies between different single molecules exceed the homogeneous linewidth by about a factor between two to five. [13, 17] For example, Kang et al. observe  $\sim 7.5 \text{ cm}^{-1}$  frequency variations in adsorbed molecules in TERS. [46] At room temperature, inhomogeneous broadening decrease to between one to two and a half times the homogeneous width. [13, 17, 39] Assuming similar dynamic broadening, this would correspond to  $2 < S_g < 5$  at low temperatures and  $1 < S_g < 2.5$  at room temperature, respectively. These values have to be seen as upper limits, because the spectral diffusion amplitude is expected to be lower than the inhomogeneous broadening.

Similar  $S_g$  may be expected based on the relationship between molecular forces and frequency shifts of anharmonic vibrational modes. Considering the model laid out by Hutchinson et. al., force fluctuations on the order of  $\approx 25\text{-}100 \text{ pN}$  may translate to  $\Delta\nu$  of  $2\text{--}5 \text{ cm}^{-1}$  for aromatic ring breathing, nitrile stretch, and CO stretching modes, corresponding to  $0.4 < S_g < 2.5$  for typical single-molecule Raman linewidths of  $2\text{--}5 \text{ cm}^{-1}$  [13, 17, 39]. These values for  $S_g$  are based on the relationship  $-F \frac{3\nu_e g}{2f^2} \approx \Delta\nu$ , where  $\nu_e$  is the unperturbed frequency, and  $f$  and  $g$  the bond's harmonic and anharmonic force constants, respectively. [47] Such fluctuating forces on the order of piconewtons can emerge from protein binding events, protein folding, and conformational switching, [48–56] and in some rare cases even nanonewton forces have been observed. [57]

The above values for  $S_g$  are also in line with studies on force-transduced Raman peak shifts in different environments. Kho et al. report force-induced SERS shifts of  $\sim 2\text{--}4 \text{ cm}^{-1}$  from molecular crowding. Finally, Mostafa et. al. report mode shifting in proteins on second timescales. The  $1269 \text{ cm}^{-1}$  mode of cytochrome C is observed to fluctuate between two values separated by  $12 \text{ cm}^{-1}$  due to a still unknown mechanism, which corresponds to  $S_d \approx 1$ . [14]

As seen in Figure 2, spectral diffusion with  $1 < S_d < 3$  may be resolved on the micro- to millisecond timescale, depending on the count rate and total integration time, reaching far into the temporal blindspot of current methods. SERS photon count are not always directly reported in the literature, but range anywhere from between 100 to 1,000,000 per second per molecule, the highest of which are reported for 'pico-cavities' formed by atomic protrusions. [20, 30, 31] The expected time-resolution of STERS is therefore highly system dependent, and will range between hundreds of nanoseconds to milliseconds. The experimental feasibility of STERS,

however, depends on prolonged experimental times, which is particularly limited in the case of the highest-enhancement factor plasmonic substrates with bright single-molecule SERS signals. Here, STERS can alleviate the issue of sample instability by either reducing the excitation power or using more robust lower enhancement factor substrates of cavities that mitigate local heating at the expense of field confinement. In this vein, STERS may enable the measurement of SERS dynamics using dielectric nanophotonics for enhancement, which have shown promise due to low heat conversion and minimal background. [58, 59].

STERS further distinguishes itself by its ability to cross-correlate different Raman spectral lines to form multidimensional spectral-fluctuation maps. Multi-dimensional STERS yields similar results as a reported coordinate analysis in TERS, but over a broader range of timescales [13]. Park et al. proposed that surface adsorption dynamics can be understood through correlation analysis, where molecular orientation on metallic surfaces anti-correlates modes with different symmetry and correlates those with the same symmetry [13]. We propose testing multi-dimensional STERS to analyze macromolecular conformational dynamics and intermolecular forces, revealing solvent exposure and force transduction between different parts of the molecule. This approach could complement 2D NMR, which lacks single-molecule sensitivity, and 2D IR spectroscopy, which has limited time resolution [60–66].

Finally, we highlight STERS’ elimination of the need to isolate strictly one molecule in the SERS hotspot. Similar to FCS, STERS can extract average single molecule dynamics even for small sub-ensembles. [67] This aspect helps overcome the common issue in SERS of reliable single-molecule placement and verification using e.g., the bi-analyte method [41, 68–70], which is prone to problems from differences in dual-analyte adsorption affinities or molecular grouping. While not providing individual single-molecule spectral fluctuations one-by-one, but rather the average single-molecule dynamics, the STERS approach still eliminates static inhomogeneous broadening and may resolve the larger issue of poor sample reproducibility of high-enhancement plasmonic substrates.

## 4. Conclusion

In conclusion, we propose a new Raman method to analyze vibrational spectral diffusion with the spectral auto- and cross-correlations between different Raman lines. STERS’ advantages may help alleviate some of the long-standing problems in SERS and provide a more accessible and reliable method for quantifying vibrational spectral diffusion, which will be of fundamental and applied interest in different fields concerned with molecular dynamics. We aim for STERS to bridge the gap between the frame-by-frame approach and ultrafast vibrational spectroscopy, the difficult-to-reach range of nanoseconds to milliseconds for the characterization of biomolecular dynamics [71–73] with single molecule SERS [13, 16, 20, 28] and in interfacial dynamics in catalysis [22, 23]. To this end, future work will focus on experimental implementation to study single-molecule dynamics in plasmonic SERS model systems, on surfaces (in catalysis and electrochemistry), as well as biophysics.

## Supporting Info

### 5. Methods: Numerical Simulations

A stream of photons, simulated with Poisson time statistics, is assigned a detector arrival time and energy based on its arrival time relative to frequency information about the emitter. The emitter frequency is assigned for all of the experimental time with a probability of switching to another value at a time  $\tau_c$ . Then, a probability of being detected at detector 1 or 2 is assigned based on the path length difference and photon energy. Once the stream of photons has all of the information about energy, detector, and arrival time, the detectors are correlated using an algorithm laid out in [74]. With a  $g_{\delta}^{(2)}(\tau)$  function for each stage position  $\delta$ , a  $\tau$  is chosen to

create the  $g_{\tau}^{(2)}(\delta)$  interferogram, which is Fourier transformed to get the spectral correlation function for all  $\tau$ . It is important to note that the true values for the FWHM may be slightly less or slightly higher than the simulated value. This is due to the number of stage positions chosen. More stage positions can be chosen to increase the spectral resolution, but this must be balanced with considerations of experimental time. this can lead to a slight under-sampling of the interferogram, which can also alter the true values of the linewidths.

We draw each photon from a Lorentzian probability distribution,  $\text{FWHM}_1$ , with some center frequency, and then after the fluctuation time, we choose a different center frequency with a probability distribution defined by a Gaussian of linewidth,  $\text{FWHM}_2$ , where the representative parameter is  $S_g$  as defined above.

## 6. Derivation of SBR

To derive the Signal to Background (SBR) ratio of STERS, the spectral correlation can first be written as:

$$p(\tau, \zeta) = \left\langle \int_{-\infty}^{\infty} s(t, \omega) s(t + \tau, \omega + \zeta) d\omega \right\rangle \equiv \langle s(t, \omega) * s(t + \tau, \omega + \zeta) \rangle \quad (8)$$

where condensed notation for the convolution is used. In a sub-ensemble of independent spectrally diffusing emitters, the overall spectrum ( $s(t, \omega)$ ) is a linear combination of multiple scatterers which allows the spectral correlation to be written like this:

$$\langle s(t, \omega) * s(t + \tau, \omega + \zeta) \rangle = \left\langle \left( \sum_{i=1}^{i=n} s_i(t, \omega) \right) * \left( \sum_{j=1}^{j=n} s_j(t + \tau, \omega + \zeta) \right) \right\rangle. \quad (9)$$

The product under the integral can be multiplied out giving separated spectral auto-correlations and cross-correlations:

$$\langle s(t, \omega) * s(t + \tau, \omega + \zeta) \rangle = \left\langle \sum_{i=j} s_i(t, \omega) * s_j(t + \tau, \omega + \zeta) \right\rangle + \left\langle \sum_{i \neq j} s_i(t, \omega) * s_j(t + \tau, \omega + \zeta) \right\rangle. \quad (10)$$

This is equivalent to

$$p(\tau, \zeta) = p(\tau, \zeta)_{\text{single molecule}} + p(\tau, \zeta)_{\text{ensemble}}. \quad (11)$$

The single-molecule spectral correlation  $p(\tau, \zeta)_{\text{single molecule}}$  and the ensemble spectral correlation  $p(\tau, \zeta)_{\text{ensemble}}$  add linearly to the total spectral correlation. From this point, it can be seen that there are  $n$  terms where  $i=j$ , therefore:

$$\text{signal} = N. \quad (12)$$

Now there also are  $N^2$  total terms, and since there are only the two cases where  $i=j$  and  $i \neq j$ , there must be  $N^2 - N$  terms such that  $i \neq j$ . These are the background terms.

$$\text{background} = N^2 - N. \quad (13)$$

This shows that the amplitude of  $p(\tau, \zeta)_{\text{single molecule}}$  relative to  $p(\tau, \zeta)_{\text{ensemble}}$  or the SBR decreases with increasing number  $N$  of simultaneously measured molecules with the relation

$$\frac{\text{signal}}{\text{background}} = \frac{p(\tau, \zeta)_{\text{single molecule}}}{p(\tau, \zeta)_{\text{ensemble}}} = \frac{1}{N - 1}. \quad (14)$$

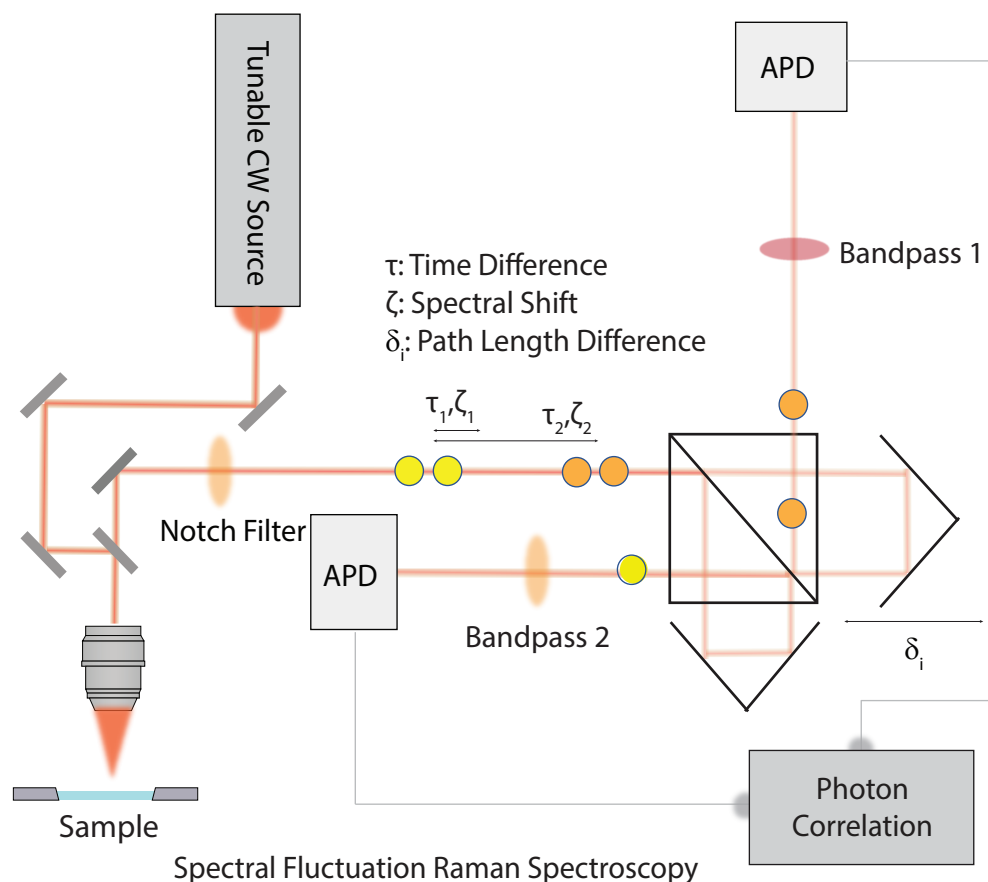


Fig. 6. Experimental schematic which includes a confocal microscope with an output coupled to a Michelson interferometer. The output of the interferometer is sent into photon counting point detectors with bandpass filters to choose the Raman mode.

## 7. Experimental Setup

### References

1. D. C. Smith and C. Carabatos-Nédelec, "Raman spectroscopy applied to crystals: phenomena and principles, concepts and conventions," PRACTICAL SPECTROSCOPY SERIES **28**, 349–422 (2001).
2. S. Praver and R. J. Nemanich, "Raman spectroscopy of diamond and doped diamond," Philos. Trans. Royal Soc. London. Ser. A: Math. Phys. Eng. Sci. **362**, 2537–2565 (2004).
3. V. Zani, D. Pedron, R. Pilot, and R. Signorini, "Contactless temperature sensing at the microscale based on titanium dioxide raman thermometry," Biosensors **11**, 102 (2021).
4. W. R. Welch, J. Kubelka, and T. A. Keiderling, "Infrared, vibrational circular dichroism, and raman spectral simulations for  $\beta$ -sheet structures with various isotopic labels, interstrand, and stacking arrangements using density functional theory," The J. Phys. Chem. B **117**, 10343–10358 (2013).
5. W. Nuansing, A. Rebollo, J. M. Mercero, *et al.*, "Vibrational spectroscopy of self-assembling aromatic peptide derivatives," J. Raman Spectrosc. **43**, 1397–1406 (2012).
6. L. Sparks, W. R. Scheidt, and J. Shelnutt, "Effects of  $\pi$ - $\pi$  interactions on molecular structure and resonance raman spectra of crystalline copper (ii) octaethylporphyrin," Inorg. Chem. **31**, 2191–2196 (1992).
7. T. Yamaguchi, Y. Kimura, and N. Hirota, "Solvent and solvent density effects on the spectral shifts and the bandwidths of the absorption and the resonance raman spectra of phenol blue," The J. Phys. Chem. A **102**, 2252–2252 (1998).
8. K. W. Kho, U. Dinis, A. Kumar, and M. Olivo, "Frequency shifts in sers for biosensing," ACS nano **6**, 4892–4902

- (2012).
9. J. T. Motz, S. J. Gandhi, O. R. Scepanovic, *et al.*, “Real-time raman system for in vivo disease diagnosis,” *J. biomedical optics* **10**, 031113–031113 (2005).
  10. D. Kurouski, R. P. Van Duyne, and I. K. Lednev, “Exploring the structure and formation mechanism of amyloid fibrils by raman spectroscopy: a review,” *Analyst* **140**, 4967–4980 (2015).
  11. W. Zhu, J. A. Hutchison, M. Dong, and M. Li, “Frequency shift surface-enhanced raman spectroscopy sensing: An ultrasensitive multiplex assay for biomarkers in human health,” *ACS sensors* **6**, 1704–1716 (2021).
  12. B. Tang, J. Wang, J. A. Hutchison, *et al.*, “Ultrasensitive, multiplex raman frequency shift immunoassay of liver cancer biomarkers in physiological media,” *ACS nano* **10**, 871–879 (2016).
  13. K.-D. Park, E. A. Muller, V. Kravtsov, *et al.*, “Variable-temperature tip-enhanced raman spectroscopy of single-molecule fluctuations and dynamics,” *Nano letters* **16**, 479–487 (2016).
  14. A. Mostafa, Y. Kanehira, K. Tapio, and I. Bald, “From bulk to single molecules: Surface-enhanced raman scattering of cytochrome c using plasmonic dna origami nanoantennas,” *Nano Lett.* (2024).
  15. A. M. Rao, P. Eklund, S. Bandow, *et al.*, “Evidence for charge transfer in doped carbon nanotube bundles from raman scattering,” *Nature* **388**, 257–259 (1997).
  16. H.-H. Shin, G. J. Yeon, H.-K. Choi, *et al.*, “Frequency-domain proof of the existence of atomic-scale sers hot-spots,” *Nano letters* **18**, 262–271 (2018).
  17. C. Artur, E. C. Le Ru, and P. G. Etchegoin, “Temperature dependence of the homogeneous broadening of resonant raman peaks measured by single-molecule surface-enhanced raman spectroscopy,” *The J. Phys. Chem. Lett.* **2**, 3002–3005 (2011).
  18. J. M. Klingsporn, N. Jiang, E. A. Pozzi, *et al.*, “Intramolecular insight into adsorbate–substrate interactions via low-temperature, ultrahigh-vacuum tip-enhanced raman spectroscopy,” *J. Am. Chem. Soc.* **136**, 3881–3887 (2014).
  19. L. A. Jakob, W. M. Deacon, R. Arul, *et al.*, “Accelerated molecular vibrational decay and suppressed electronic nonlinearities in plasmonic cavities through coherent raman scattering,” *Phys. Rev. B* **109**, 195404 (2024).
  20. M. M. Schmidt, E. A. Farley, M. A. Engevik, *et al.*, “High-speed spectral characterization of single-molecule sers fluctuations,” *ACS nano* **17**, 6675–6686 (2023).
  21. N. Chiang, X. Chen, G. Goubert, *et al.*, “Conformational contrast of surface-mediated molecular switches yields ångstrom-scale spatial resolution in ultrahigh vacuum tip-enhanced raman spectroscopy,” *Nano letters* **16**, 7774–7778 (2016).
  22. C. M. Zoltowski, D. N. Shoup, and Z. D. Schultz, “Investigation of sers frequency fluctuations relevant to sensing and catalysis,” *The J. Phys. Chem. C* **126**, 14547–14557 (2022).
  23. H.-K. Choi, W.-H. Park, C.-G. Park, *et al.*, “Metal-catalyzed chemical reaction of single molecules directly probed by vibrational spectroscopy,” *J. Am. Chem. Soc.* **138**, 4673–4684 (2016).
  24. P. G. Etchegoin and E. C. Le Ru, “Resolving single molecules in surface-enhanced raman scattering within the inhomogeneous broadening of raman peaks,” *Anal. chemistry* **82**, 2888–2892 (2010).
  25. S. Yampolsky, D. A. Fishman, S. Dey, *et al.*, “Seeing a single molecule vibrate through time-resolved coherent anti-stokes raman scattering,” *Nat. Photonics* **8**, 650–656 (2014).
  26. P. Kukura, D. W. McCamant, and R. A. Mathies, “Femtosecond stimulated raman spectroscopy,” *Annu. Rev. Phys. Chem.* **58**, 461–488 (2007).
  27. A. Tokmakoff and M. Fayer, “Homogeneous vibrational dynamics and inhomogeneous broadening in glass-forming liquids: Infrared photon echo experiments from room temperature to 10 k,” *The J. chemical physics* **103**, 2810–2826 (1995).
  28. H. Arnolds and M. Bonn, “Ultrafast surface vibrational dynamics,” *Surf. Sci. Reports* **65**, 45–66 (2010).
  29. A. E. Bragg, W. Yu, J. Zhou, and T. Magnanelli, “Ultrafast raman spectroscopy as a probe of local structure and dynamics in photoexcited conjugated materials,” *The journal physical chemistry letters* **7**, 3990–4000 (2016).
  30. N. C. Lindquist, C. D. L. de Albuquerque, R. G. Sobral-Filho, *et al.*, “High-speed imaging of surface-enhanced raman scattering fluctuations from individual nanoparticles,” *Nat. nanotechnology* **14**, 981–987 (2019).
  31. M. Kamp, B. de Nijs, N. Kongsuwan, *et al.*, “Cascaded nanooptics to probe microsecond atomic-scale phenomena,” *Proc. National Acad. Sci.* **117**, 14819–14826 (2020).
  32. X. Brokmann, M. Bawendi, L. Coolen, and J.-P. Hermier, “Photon-correlation fourier spectroscopy,” *Opt. express* **14**, 6333–6341 (2006).
  33. H. Utzat, W. Sun, A. E. Kaplan, *et al.*, “Coherent single-photon emission from colloidal lead halide perovskite quantum dots,” *Science* **363**, 1068–1072 (2019).
  34. B. Spokoyny, H. Utzat, H. Moon, *et al.*, “Effect of spectral diffusion on the coherence properties of a single quantum emitter in hexagonal boron nitride,” *The journal physical chemistry letters* **11**, 1330–1335 (2020).
  35. J. Cui *et al.*, “Deconstructing the room-temperature emission spectra of nanocrystals using photon-correlation fourier spectroscopy,” Ph.D. thesis, Massachusetts Institute of Technology (2014).
  36. M. Peters, T. Zhao, S. George, *et al.*, “Energy landscape of conformational changes for a single unmodified protein,” *npj Biosensing* **1**, 14 (2024).
  37. W. Ye, M. Gotz, S. Celiksoy, *et al.*, “Conformational dynamics of a single protein monitored for 24 h at video rate,” *Nano letters* **18**, 6633–6637 (2018).
  38. H. Utzat and M. G. Bawendi, “Lifetime-resolved photon-correlation fourier spectroscopy,” *Opt. Express* **29**, 14293–14303 (2021).

39. S. George, A. Harris, M. Berg, and C. Harris, "Picosecond studies of the temperature dependence of homogeneous and inhomogeneous vibrational linewidth broadening in liquid acetonitrile," (1983).
40. F. A. Nia, *Probing Molecular Kinetics Using Higher-Order Fluorescence Correlation Spectroscopy* (Colorado State University, 2019).
41. E. Blackie, E. Le Ru, M. Meyer, *et al.*, "Bi-analyte sers with isotopically edited dyes," *Phys. Chem. Chem. Phys.* **10**, 4147–4153 (2008).
42. S. Saffarian and E. L. Elson, "Statistical analysis of fluorescence correlation spectroscopy: the standard deviation and bias," *Biophys. journal* **84**, 2030–2042 (2003).
43. M. D. Sonntag, D. Chulhai, T. Seideman, *et al.*, "The origin of relative intensity fluctuations in single-molecule tip-enhanced raman spectroscopy," *J. Am. Chem. Soc.* **135**, 17187–17192 (2013).
44. N. Demirdöven, M. Khalil, O. Golonzka, and A. Tokmakoff, "Correlation effects in the two-dimensional vibrational spectroscopy of coupled vibrations," *The J. Phys. Chem. A* **105**, 8025–8030 (2001).
45. S. A. Bhat and S. Ahmad, "Ftir, ft-raman and uv–vis spectral studies of d-tyrosine molecule," *J. Mol. Struct.* **1105**, 169–177 (2016).
46. M. Kang, H. Kim, E. Oleiki, *et al.*, "Conformational heterogeneity of molecules physisorbed on a gold surface at room temperature," *Nat. Commun.* **13**, 4133 (2022).
47. E. J. Hutchinson and D. Ben-Amotz, "Molecular force measurement in liquids and solids using vibrational spectroscopy," *The J. Phys. Chem. B* **102**, 3354–3362 (1998).
48. C. J. Bustamante, Y. R. Chemla, S. Liu, and M. D. Wang, "Optical tweezers in single-molecule biophysics," *Nat. Rev. Methods Primers* **1**, 25 (2021).
49. E.-L. Florin, V. T. Moy, and H. E. Gaub, "Adhesion forces between individual ligand-receptor pairs," *Science* **264**, 415–417 (1994).
50. M. S. Kellermayer, S. B. Smith, H. L. Granzier, and C. Bustamante, "Folding-unfolding transitions in single titin molecules characterized with laser tweezers," *Science* **276**, 1112–1116 (1997).
51. M. Rief, M. Gautel, F. Oesterhelt, *et al.*, "Reversible unfolding of individual titin immunoglobulin domains by afm," *science* **276**, 1109–1112 (1997).
52. J.-Y. Shao, H. P. Ting-Beall, and R. M. Hochmuth, "Static and dynamic lengths of neutrophil microvilli," *Proc. National Acad. Sci.* **95**, 6797–6802 (1998).
53. T. R. Strick, J.-F. Allemand, D. Bensimon, *et al.*, "The elasticity of a single supercoiled dna molecule," *Science* **271**, 1835–1837 (1996).
54. T. Strick, J.-F. Allemand, D. Bensimon, and V. Croquette, "Stress-induced structural transitions in dna and proteins," *Annu. review biophysics biomolecular structure* **29**, 523–543 (2000).
55. L. Tskhovrebova, J. Trinick, J. Sleep, and R. Simmons, "Elasticity and unfolding of single molecules of the giant muscle protein titin," *Nature* **387**, 308–312 (1997).
56. M. Akamatsu, R. Vasan, D. Serwas, *et al.*, "Principles of self-organization and load adaptation by the actin cytoskeleton during clathrin-mediated endocytosis," *Elife* **9**, e49840 (2020).
57. M. Jasnin, J. Hervy, S. Balor, *et al.*, "Elasticity of podosome actin networks produces nanonewton protrusive forces," *Nat. Commun.* **13**, 3842 (2022).
58. J. Cambiasso, M. König, E. Cortes, *et al.*, "Surface-enhanced spectroscopies of a molecular monolayer in an all-dielectric nanoantenna," *Acs Photonics* **5**, 1546–1557 (2018).
59. M. Caldarola, P. Albella, E. Cortés, *et al.*, "Non-plasmonic nanoantennas for surface enhanced spectroscopies with ultra-low heat conversion," *Nat. communications* **6**, 7915 (2015).
60. L. E. Kay, D. A. Torchia, and A. Bax, "Backbone dynamics of proteins as studied by nitrogen-15 inverse detected heteronuclear nmr spectroscopy: application to staphylococcal nuclease," *Biochemistry* **28**, 8972–8979 (1989).
61. A. G. Palmer III, M. Rance, and P. E. Wright, "Intramolecular motions of a zinc finger dna-binding domain from xfn characterized by proton-detected natural abundance carbon-13 heteronuclear nmr spectroscopy," *J. Am. Chem. Soc.* **113**, 4371–4380 (1991).
62. N. A. Farrow, R. Muhandiram, A. U. Singer, *et al.*, "Backbone dynamics of a free and a phosphopeptide-complexed src homology 2 domain studied by 15n nmr relaxation," *Biochemistry* **33**, 5984–6003 (1994).
63. M. T. Zanni, "Two-dimensional infrared spectroscopy measures the structural dynamics of a self-assembled film only one molecule thick," *Proc. National Acad. Sci.* **113**, 4890–4891 (2016).
64. J. Lim, K.-K. Lee, C. Liang, *et al.*, "Two-dimensional infrared spectroscopy and molecular dynamics simulation studies of nonaqueous lithium ion battery electrolytes," *The J. Phys. Chem. B* **123**, 6651–6663 (2019).
65. D. C. Urbanek, D. Y. Vorobyev, A. L. Serrano, *et al.*, "The two-dimensional vibrational echo of a nitrile probe of the villin hp35 protein," *The journal physical chemistry letters* **1**, 3311–3315 (2010).
66. Z. Ganim, H. S. Chung, A. W. Smith, *et al.*, "Amide i two-dimensional infrared spectroscopy of proteins," *Accounts chemical research* **41**, 432–441 (2008).
67. S. T. Hess, S. Huang, A. A. Heikal, and W. W. Webb, "Biological and chemical applications of fluorescence correlation spectroscopy: a review," *Biochemistry* **41**, 697–705 (2002).
68. P. G. Etchegoin, E. C. Le Ru, and A. Fainstein, "Bi-analyte single molecule sers technique with simultaneous spatial resolution," *Phys. Chem. Chem. Phys.* **13**, 4500–4506 (2011).
69. J. A. Dieringer, R. B. Lettan, K. A. Scheidt, and R. P. Van Duyne, "A frequency domain existence proof of single-molecule surface-enhanced raman spectroscopy," *J. Am. Chem. Soc.* **129**, 16249–16256 (2007).

70. E. C. Le Ru, M. Meyer, and P. G. Etchegoin, "Proof of single-molecule sensitivity in surface enhanced raman scattering (sers) by means of a two-analyte technique," *The journal physical chemistry B* **110**, 1944–1948 (2006).
71. A. Abyzov, M. Blackledge, and M. Zweckstetter, "Conformational dynamics of intrinsically disordered proteins regulate biomolecular condensate chemistry," *Chem. Rev.* **122**, 6719–6748 (2022).
72. P. Campitelli, T. Modi, S. Kumar, and S. B. Ozkan, "The role of conformational dynamics and allostery in modulating protein evolution," *Annu. review biophysics* **49**, 267–288 (2020).
73. J. Guo and H.-X. Zhou, "Protein allostery and conformational dynamics," *Chem. reviews* **116**, 6503–6515 (2016).
74. T. A. Laurence, S. Fore, and T. Huser, "Fast, flexible algorithm for calculating photon correlations," *Opt. letters* **31**, 829–831 (2006).